A Linear Permanent Magnet Synchronous Motor for Large Volume Needle-free Jet Injection

Nick N. L. Do
Auckland Bioengineering Institute
The University of Auckland
70 Symonds Street, Auckland 1010, New Zealand
Email: ldo004@aucklanduni.ac.nz

Andrew J. Taberner and Bryan P. Ruddy
Department of Engineering Science
and Auckland Bioengineering Institute
The University of Auckland
70 Symonds Street, Auckland 1010, New Zealand
Email: a.taberner@auckland.ac.nz; b.ruddy@auckland.ac.nz

Abstract—Needle-free jet injection allows delivery of liquid drugs through the skin in the form of a narrow fluid jet traveling at high speed, minimizing the risk of accidents. The use of a controllable actuator to drive this process has many advantages, but the voice coil actuators previously used are too large and heavy for practical use with common injection volumes (1 mL). We instead propose a compact slotless tubular linear permanent magnet synchronous motor design for jet injection. The design was determined by utilizing a semi-analytical electromagnetic modeling technique to predict the performance of any given motor design, an optimization scheme for the motor mass at a given power dissipation, and an automated routine for estimating cogging force using finite-element analysis. A prototype motor was constructed, with a nominal mass of 322 g, a stroke of 80 mm, and a target operating power of 1.2 kW; experimental data show that the motor constant is within 10% of the target, and that the cogging force is in close agreement with the model. Test ejection of water into a force sensor verified that the motor is fit for needle-free injection. The design methodology explained here shows the benefits to integrated design optimization of both the actuator and the load, particularly in systems that drive fluid pressure loads, and also opens the door to controllable injector designs for larger volumes.

Index Terms—Drug delivery, design optimization, electromechanical systems, actuators, linear permanent magnet synchronous motor, magnetic fields.

I. INTRODUCTION

Needle free jet injection (NFJI) is a safe and efficient method of transdermal drug delivery, which can be realized by forcing a fluid jet of $76\,\mu m - 360\,\mu m$ diameter to penetrate the skin at a jet speed v which is typically faster than 100 m/s [1]. Most commercially available jet injectors are mechanically powered. This type of device offers limited control over injection depth and jet velocity, which can result in occasional bruising and other adverse effects. Recent advances in direct-drive linear actuators have enabled the realization of successful prototypes of electronically controlled jet injectors [2], [3]. They introduced the advantage of superior repeatability using real-time jet velocity control at a bandwidth higher than 1 kHz [4].

The requirements for jet injectors powered by electric motors are demanding. Usability of handheld injectors is heavily constrained by the motor mass, while the actuation profile demands very high pulse force at near-stall velocity. So far, existing prototypes have relatively heavy weights and large
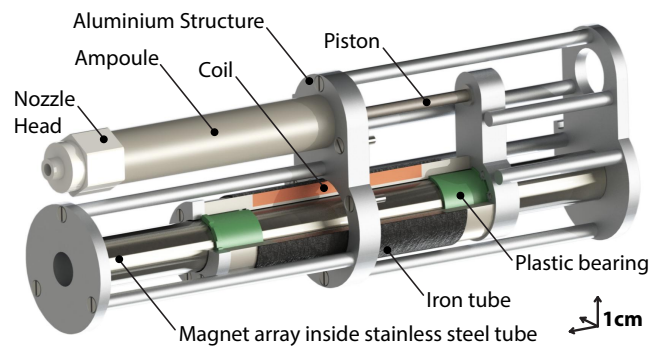

Fig. 1. Cut-away view of the optimized motor and jet injector design, showing the bobbin and coil riding on linear plastic bearings along the magnet array, as well as the supporting structure, piston, and drug ampoule.

sizes for small drug injection volumes. For instance, the voice coil actuator described in [5] has a total mass of $300\,\text{g}$, but is only able to drive an injection volume of up to $300\,\mu L$.

There are reports on modeling and optimization approaches for developing direct-drive linear motors for this role: voice coil motors (VCMs) based on quasi-Halbach topology [5] and slotless tubular linear permanent magnet synchronous motors (LPMSMs) [6].

The scaling law for NFJI VCMs [5] states that, for a given fixed electrical input power P, the required mass M grows faster than the injection volume V, with $M \propto V^{6/5}$. To provide a $1\,\text{mL}$ injection, then, a voice coil actuator of over $1\,\text{kg}$ mass would be required, which is not practical for a hand-held device. Thus, a new form of injection ampoule [7] was conceived to break this scaling relationship by providing different piston diameters for the two phases of NFJI [8]; however, this mechanical decoupling approach is inefficient and has limited flexibility.

LPMSMs, on the other hand, are not subjected to the coupling between motor stroke and performance seen in VCMs. Significant power efficiency gains from using this type of motor are possible, if the motor length can be long. However, the hand-held nature of jet injection devices does not readily allow for this trade-off.

In this paper, we describe a semi-analytical electromagnetic model for slotless tubular LPMSMs, following from that
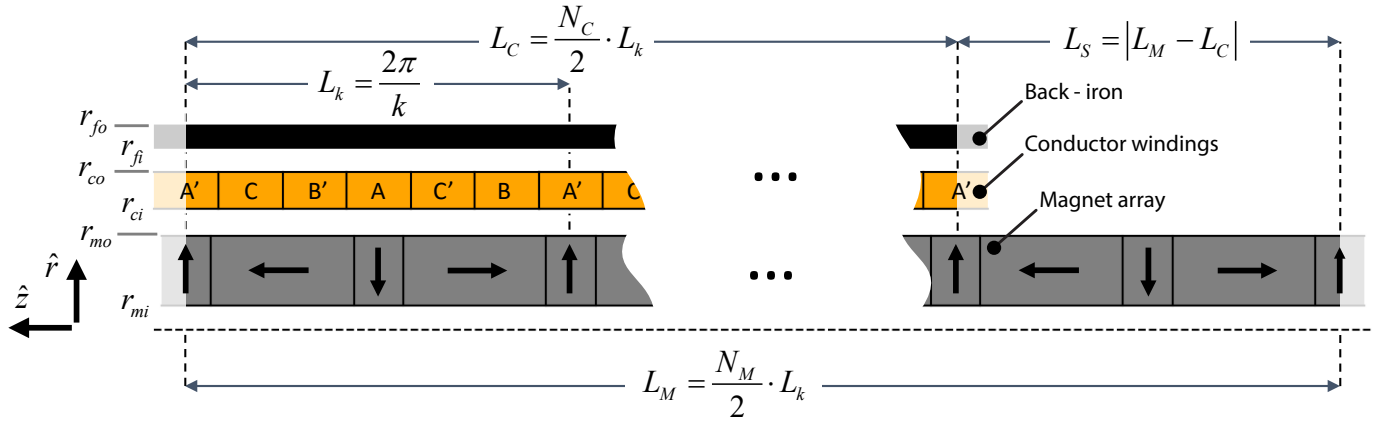
Fig. 2. This schematic illustrates a tubular LPMSM with quasi-Halbach magnets, slotless windings, and a shortened exterior back-iron tube. The radii of magnet, coil, and back are shown; the structure has periodicity with wavenumber k, wave length L_k, number of half coil poles N_C and half magnet poles N_M. The arrows indicate direction of magnetization of magnets, while the characters label the coil phases.

presented in [6]. We then present an optimization scheme for the motor mass at a given power dissipation and an automated routine for estimating cogging force using finite-element analysis (FEA). Using these methods, we constructed and preliminarily tested an optimized and practical LPMSM motor design for NFJI in [9]. Validation of this actuator for NFJI will be introduced and discussed in this paper. Fig. 1 shows a render of the mechanical design concept for the finalized motor configuration.

II. ELECTROMAGNETIC MODEL

Our modeling approach is outlined in [10] and employed in [5], [6]: an analytical Fourier series solution was used to solve Poisson's equation in cylindrical coordinates directly. This formulation provides a good tradeoff between accuracy and computational efficiency. It computes faster compared to FEA [11] or the standard integral formulation [12], [13] and avoids the problems of numerical instability exhibited by other explicit analytical solutions [14], [15].

Based on [5], we will study a slight variation of this topology using a shorter exterior back-iron. In this approach, the back-iron only covers the coil and travels along with it, as shown in Fig. 2. The advantage of shortened back-iron over using iron to cover the entire motor length is the reduction in weight, which is an important objective in designing hand-held devices. However, a moving-iron configuration introduces cogging effects that can be problematic for smooth motion control.

Ignoring resistance due to fluid viscosity, the actuator force F and jet speed v have the following relation:

$$F = \frac{\pi}{8} \rho v^2 D^2 \tag{1}$$

where ρ is the density of fluid being delivered and D is the diameter of the piston cylinder. For linear permanent magnet motors, the motor constant K_m, measured in $N/\sqrt{W}$, is a measure of force production efficiency that is independent of the winding properties. We can combine these relationships

to find the power dissipation in the motor windings P for a given ampoule volume V and length of piston travel L_s:

$$P = \frac{\rho^2 V^2 v^4}{4 K_m^2 L_s^2} \tag{2}$$

It was shown in [10] that $K_m \propto \hat{K}_m \sqrt{M}$, where $\hat{K}_m$ is a dimensionless parameter describing the internal magnetic and electric geometry of the motor. Thus, neglecting material properties, we can determine the overall scaling behavior of motors for the needle free jet injection task:

$$P \propto \frac{V^2 v^4}{M L_s^2 \hat{K}_m^2} \tag{3}$$

Typically the application determines ρ, V, v, and L_s (or D). Thus, either motor mass M must be fixed to search for a motor with the optimum power consumption P, or P must be fixed to find a motor with the optimum motor mass.

We analyzed a motor with repeat units of coil and magnet of wavelength L_k, ratio of radial magnet length over a pair of radial-axial magnet δ, coil length L_C, magnet length L_M, and arbitrary number of half coil poles N_C and magnet poles N_M, as illustrated in Fig. 2. The motor is overhung if $N_C > N_M$, and underhung if $N_M > N_C$. Previous research in [6] points out that underhung motors offer superior efficiency to overhung motors; thus, only underhung motors are considered here. The length of the motor simplifies to:

$$L_{motor} \equiv L_M = \frac{N_M}{2} \cdot L_k \tag{4}$$

The magnetization of permanent magnets can be represented by a Fourier series where $\hat{M}_{rn}$ and $\hat{M}_{zn}$ are the dimensionless radial and axial magnetizations, respectively, in odd harmonic order:

$$\hat{M}_{rn} = \frac{4 N_{seg}}{n\pi^2} \sin\left(\frac{\pi}{N_{seg}}\right) \sin\left(\frac{n\pi\delta}{2}\right) \tag{5}$$

$$\hat{M}_{zn} = -\frac{4}{n\pi^2}\cos\left(\frac{n\pi\delta}{2}\right) \tag{6}$$

Uniformly magnetized segments are used in place of each radial magnet to approximate true radial magnetization. This imperfection is also accounted for in the model by a method of analyzing 3D effects in a segmented Halbach array [16].

Valid for idealized back-iron with constant permeability, the solutions to Maxwell's equations for this set of boundary conditions can be described in terms of auxiliary functions Λ_ν based on the modified Struve function $L_\nu(x)$, and the modified Bessel functions $I_\nu(x)$, and $K_\nu(x)$:

$$\Lambda_\nu(x) \equiv \frac{\pi}{2}\left(I_\nu(x) - L_\nu(x)\right) \tag{7}$$

$$\mathcal{L}_I \equiv x\left(\Lambda_1(x)I_0(x) - \Lambda_0(x)I_1(x)\right) \tag{8}$$

$$\mathcal{L}_K \equiv x\left(\Lambda_1(x)K_0(x) + \Lambda_0(x)K_1(x)\right) \tag{9}$$

The force F can be found by determining a dimensionless force constant $\hat{F}$. We compute $\hat{F}$ by integrating the Lorentz force over the coil:

$$\hat{F} = \pi\left(\hat{a}_{1c}\hat{b}_{1m} + \hat{a}_{1m}\hat{b}_{1c}\right) \tag{10}$$

where $\hat{a}_{1m}$ and $\hat{b}_{1m}$ are the magnetic field coefficients governed by matching boundary conditions for the first harmonic, and $\hat{a}_{1c}$ and $\hat{b}_{1c}$ are parameters controlled by the coil radii. The force F can then be obtained from the dimensionless force constant,

$$F = \frac{2\pi B_{rem}J_1 N_M}{k^3}\hat{F} \tag{11}$$

where J_1 is the magnitude of the first harmonic of current density. In a similar manner, power dissipation P and motor mass M can also be non-dimensionalized:

$$\hat{P} = \frac{\pi}{2}\left[(kr_{ci})^2 - (kr_{co})^2\right] \tag{12}$$

$$P = \frac{2\pi N_M J_1^2}{\sigma k^3}\hat{P} \tag{13}$$

$$M = \frac{2\pi N_M \sigma_c}{k^3}\hat{M} \tag{14}$$

$$M = M_{coil} + M_{magnet} + M_{iron} \tag{15}$$

$$\hat{M} = \pi\left[f + (1-f)\frac{\rho_{ins}}{\rho_c}\right]\left[(kr_{co})^2 - (kr_{ci})^2\right]\left(\frac{N_C}{N_M}\right)$$
$$+\pi\left(\frac{\rho_m}{\rho_c}\right)\left[(kr_{mo})^2 - (kr_{mi})^2\right]$$
$$+\pi\left(\frac{\rho_f}{\rho_c}\right)\left[(kr_{fo})^2 - (kr_{fi})^2\right]\left(\frac{N_C}{N_M}\right) \tag{16}$$

where f is copper volume fill factor, ρ_{ins} is insulator density, ρ_c is conductor density, ρ_m is magnet volumetric

density, and ρ_f is iron density. Note that in the description of dimensionless mass $\hat{M}$ the length of the back-iron follows the length of the coil. However, back-iron length will need to be adjusted to minimize end cogging effects, which will slightly increase the total mass.

With the field solution for an infinitely permeable back-iron a_{nm}, b_{nm}, and the maximum allowed flux density B_{sat} [5], the back-iron outer radii r_{fo} can be constrained using the relationship:

$$r_{fo} = \sqrt{r_{fi}^2 + r_{fi}\frac{B_{rem}}{B_{sat}}\sum_{i=1}^{n}\frac{2\sin(\frac{n\pi}{2})}{nk}\Psi} \tag{17}$$

$$\Psi = a_{nm}I_1(nkr_{fi}) + b_{nm}K_1(nkr_{fi}) \tag{18}$$

With σ as is the conductivity of the conductor, w as the winding factor, and N_ϕ as the number of winding phases, the dimensionless motor constant $\hat{K}_m$ and the motor constant K_m can be obtained via:

$$w = \frac{2N_\phi}{\pi}\sin\left(\frac{\pi}{2N_\phi}\right) \tag{19}$$

$$K_m = B_{rem}\hat{K}_m\sqrt{\frac{\sigma M}{\rho_c}} \tag{20}$$

$$\hat{K}_m = w\hat{F}\sqrt{\frac{f}{(\frac{N_M}{N_C})\hat{P}\hat{M}}} \tag{21}$$

III. DESIGN & OPTIMIZATION

A. Requirements

Functionality and usability requirements were identified by considering the use of a handheld device:

- The device needs to deliver $V = 1\,\mathrm{mL}$ volume of fluid at a peak jet speed of $200\,\mathrm{m/s}$ ($200\,\mu m$ nozzle diameter);
- Theoretical peak power consumption P at the peak jet speed to be less than $1.2\,\mathrm{kW}$ (the motor driver will consume more to overcome friction)
- The total length of the device should not exceed $20\,\mathrm{cm}$ (including the mechanical structure and ampoule);
- The motor must weigh less than $350\,\mathrm{g}$

The target jet speed of $200\,\mathrm{m/s}$ was chosen to be adequate to overcome viscous losses in drug injection orifices while leading to practical ($100\,\mathrm{m/s}$ to $150\,\mathrm{m/s}$) injection velocities [1], while the power consumption of $1.2\,\mathrm{kW}$ is within the capability of practical self-contained power sources and power electronic drives. The duration of a typical injection is $< 0.5\,\mathrm{s}$, so heat dissipation during an injection is of minimal concern.

The mechanical design concept required the Halbach magnet array to fit inside a thin tube of austenitic stainless steel, which in turn, slides against plastic bearings. Due to the availability of parts, we constrained $r_{mo} = 7.8\,\mathrm{mm}$ to allow the use of thin stainless steel tubing of $16\,\mathrm{mm}$ outside diameter. Furthermore, we chose to use standard precision austenitic stainless steel rods to reduce the machining work

for the piston. Working back from the required volume V, the minimum stroke length L_s is 140 mm, 80 mm, and 50 mm for piston diameter or ampoule inner diameter of 3 mm, 4 mm, and 5 mm, respectively.

B. Design optimization

Based upon our previous development of power systems for jet injection [17], it was determined that the power electronics could support 1200 W of nominal motor power, with adequate margins, and with this new requirement, we focus on minimizing the mass of the motor that would meet all the requirements. Since N_M and N_C were the only parameters subjected to integer constraints, each pair of N_M and N_C was treated as an independent non-linear optimization problem. In order to find a solution for this mixed-integer optimization problem, we used a method that can be divided into an outer optimization loop and an inner optimization routine. Fig. 3 summarizes and illustrates the optimization algorithm.

In a bird's eye view, the outer optimization loop executes a strategic repetition of the inner optimization routine. The inner optimization routine searches for the most power-efficient motor configuration at each given N_{Mi}, N_{Ci}, and M_i. The inner optimization problem is convex, and readily converges to a solution. The outer loop performs a grid search across a localized region in the (N_M, N_C) space, repeated around the optimum point until that optimum lies in the center of the search grid. This approach overcomes an observed lack of local convexity in terms of N_M and N_C, by using a larger search grid than the scale of the non-convexity. This means that the program can gradually approach the best combination of N_M and N_C without getting stuck in numerous local minima. The results discussed later in Section III-C and Fig. 4(b) proved that is the case.

In the very first round, the outer optimization routine first chooses an initial mass $M_0 = m_0$ and starts searching for the most power efficient motor that it can possibly achieve in the grid of $(N_M : 0 \rightarrow 9) \times (N_C : 0 \rightarrow 9)$. Each execution of outer optimization loop runs at most a hundred inner optimizations at a time in each grid search of $(N_{M:start} \rightarrow N_{M:start} + 9) \times (N_{C:start} \rightarrow N_{C:start} + 9)$, excluding overhung configurations (when $N_C \geq N_M$). After each grid search, the outer optimization loop identifies the most power efficient motor configuration so far to obtain the period numbers $N_{M\beta}$, $N_{C\beta}$. The search stops once this motor configuration with power consumption P is found to be near enough to the desired power. If this motor configuration has not met the power requirement, the next grid search takes $N_{M\beta}$, $N_{C\beta}$ as its new center for the next grid search $(N_{M:start} = N_{M\beta} - 5, N_{C:start} = N_{C\beta} - 5)$, and the M_i set point in the outer optimization is increased by a small amount $(M_i = M_{i-1} + \text{small increment})$. In this approach, the mass M allowed in the motor search is increasing, while the power consumption P of motor configurations found by inner optimization is decreasing to approach the desired power.

To get a realistic motor configuration, material properties, design constants and constraints were introduced. A fill factor

TABLE I
SUMMARY OF MOTOR OPTIMIZATION CONSTANTS AND CONSTRAINTS

Parameter	Description	Values
V	Maximum injection volume	1 mL
v	Nominal jet speed	200 m/s
$r_{co} - r_{ci}$	Coil thickness	≥ 4 mm
r_{mo}	Fixed outer magnet array outer radius	7.8 mm
r_{mi}	Magnet array radius	≥ 2 mm
gap_{mc}	Magnet and coil fixed radial gap	1.3 mm
gap_{cf}	Coil and iron fixed radial gap	0.1 mm
L_k	Period length	≥ 12 mm
δ	Ratio of radial magnet over a period	$1 > \delta > 0$
N_M, N_C	Number of half magnet & coil phases	$\in \mathbb{N}$
$N_M - N_C$	Underhung (> 0) or Overhung (< 0)	> 0
M	Motor mass	≤ 350 g
L_s/d_s	Stroke lengths and diameter sets	140 mm / 3 mm
		80 mm / 4 mm
		50 mm / 5 mm

of 62 % was assumed for the copper conductor, and the back-iron was selected to be made of plain 1018 carbon steel. We chose to construct radial magnets from 4 segments and used $B_{sat} = 2$ T to avoid saturation in the back-iron. The back-iron thickness was calculated using 11 harmonics of the magnetic field, while the force constant was calculated from the first harmonic alone. We set the clearance gap between the magnet and coil $gap_{mc} \equiv r_{ci} - r_{mo} = 1.3$ mm to facilitate some rigidity for the bobbin shell, and the gap between coil and back-iron $gap_{cf} \equiv r_{fi} - r_{co} = 0.1$ mm to increase ease of assembly. Table I summarizes the optimization constraints for the desired motor configuration. To reduce coupling between the radial dimensions, the thicknesses of the coil $t_c = r_{co} - r_{ci}$ and of the magnets $t_m = r_{mo} - r_{mi}$ were used in the optimization, instead of r_{co} and r_{mo}. The five parameters for optimization were L_k, r_{mi}, t_m, t_c, and δ. The parameters were also subjected to additional constraints: a minimum copper thickness of $\text{Min}(t_c) = 4$ mm to guarantee the structural integrity of the bobbin, outer magnet radii $r_{mo} = t_m + r_{mi} = 7.8$ mm as noted above, a minimum inner magnet radius $\text{Min}(r_{mi}) = 2$ mm to allow for structural support through the center of the magnet array, and minimum period length $\text{Min}(L_k) = 12$ mm to make coil winding more practical. Table I summarizes the motor optimization constants and constraints.

The inner optimization routine uses constrained nonlinear multi-variable optimization based on the interior point algorithm (MATLAB Optimization Toolbox) to minimize power dissipation P, calculated via (2), (20), and (21). Many inner optimizations will be completed before the program can find the suitable motor. Across the inner optimization rounds, the following constraints are used:

- Design constants such as injection volume V, jet speed v, gap_{mc}, gap_{cf}, stroke length L_s, and piston diameter
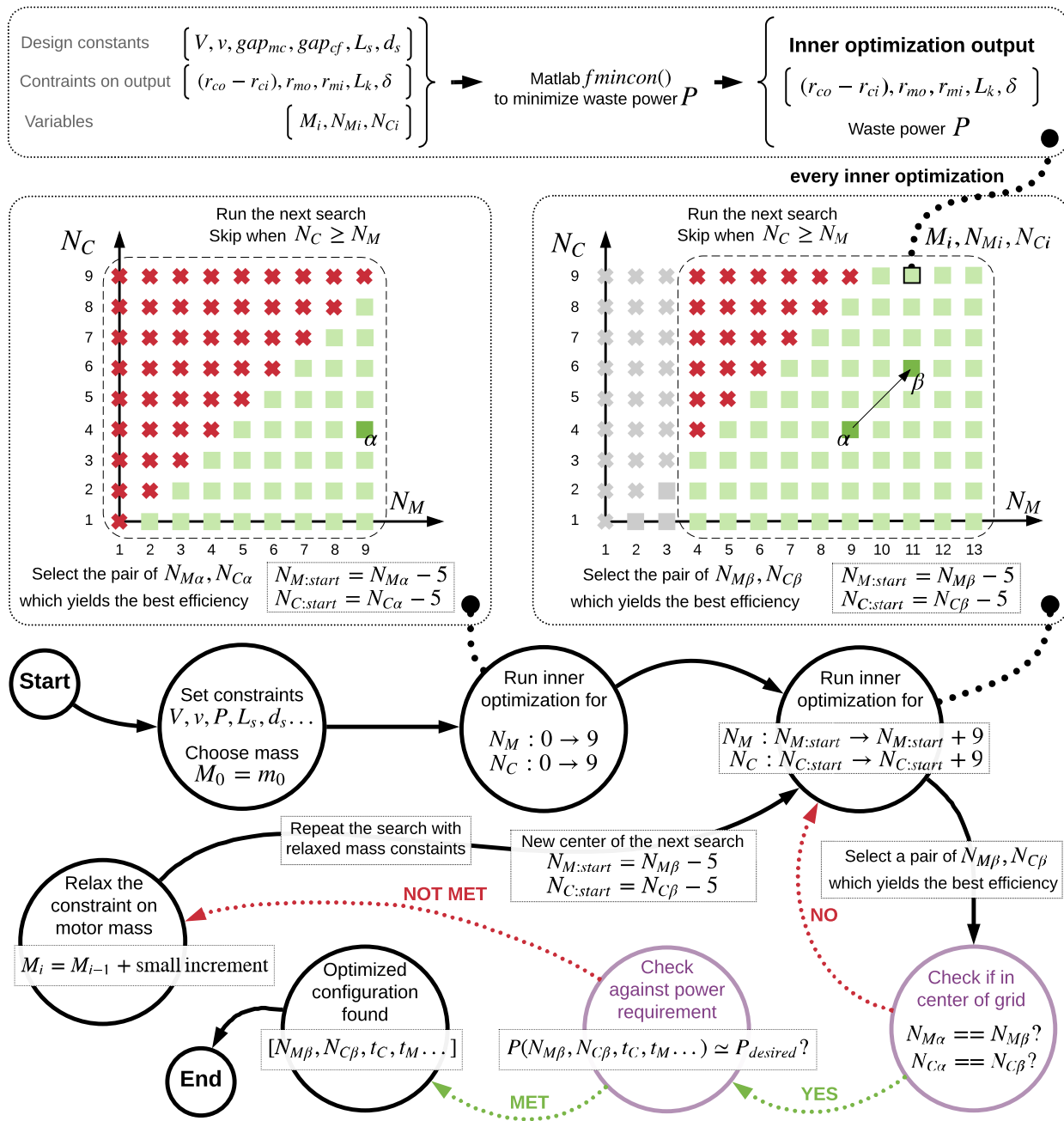
Fig. 3. Summary of the top-level motor optimization algorithm and inner optimization routine. The algorithm uses motor specifications V, v, L_s, and $P_{desired}$ to determine the motor parameters L_k, r_mi, t_m, t_c, δ, N_C, N_M and motor mass M at which all specifications are satisfied.

d_s are fixed;

- Constraints on the optimization output parameters (L_k, r_{mi}, t_m, t_c, and δ) always apply;
- Variables such as N_M, N_C, and motor mass M are up to the outer optimization loop to specify.

C. Selecting motor configuration

To see the effect of stroke length on the performance that can be obtained, Fig. 4(a) plots P_{max} against M for three stroke lengths $L_s = 50\,\text{mm}/80\,\text{mm}/140\,\text{mm}$, using

$V = 1\,\text{mL}$, $v = 200\,\text{m/s}$, $P_{max} = 1.2\,\text{kW}$ and other constraints. Although optimized motors with $140\,\text{mm}$ stroke can offer superior performance given the same motor mass M, the overall motor length L_{motor} required was found to be longer than $300\,\text{mm}$. This result agrees strongly with the previous study in [7]: PMLSMs can be more efficient if the motor length is allowed to be longer. However, with the ergonomics of the final handheld device in mind, only motors with $L_s = 80\,\text{mm}$ appear to be feasible within both the motor mass and motor length limits stated in Section III-A.
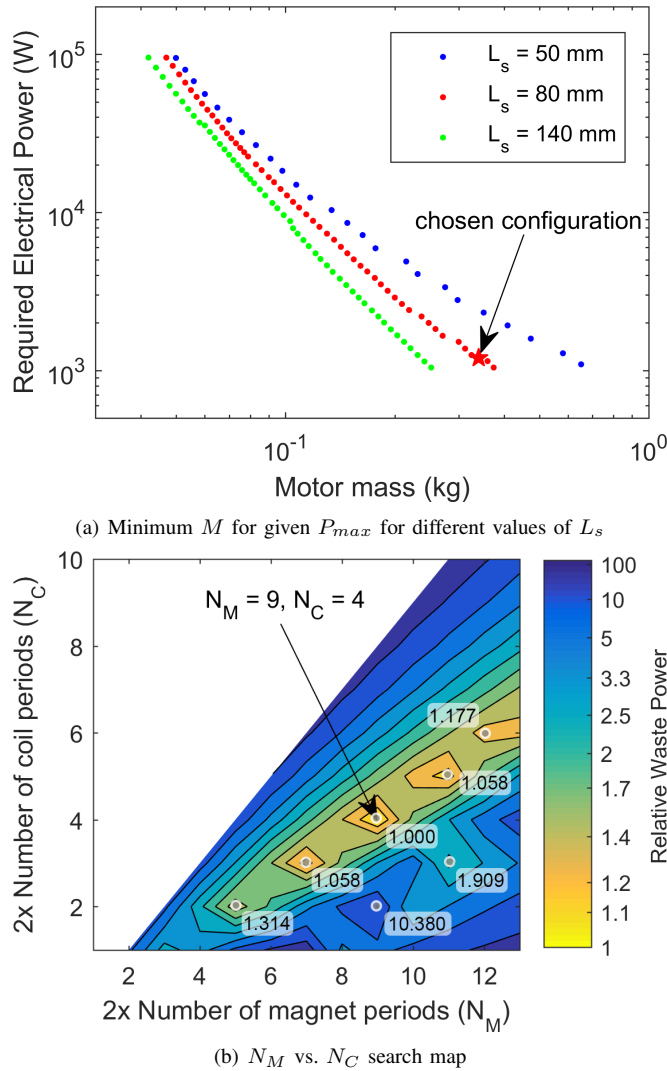
(a) Minimum M for given P_{max} for different values of L_s

(b) N_M vs. N_C search map

Fig. 4. The $(N_{M:start} \rightarrow N_{M:end}) \times (N_{C:start} \rightarrow N_{C:end})$ search map for a motor with $V = 1\,\text{mL}$, $v = 200\,\text{m/s}$, $P_{max} = 1.2\,\text{kW}$, and $L_s = 80\,\text{mm}$ yields the least motor mass at $N_M = 9$ and $N_C = 4$ as shown in (a); and plot of P_{max} against M for different stroke length L_s under the conditions $V = 1\,\text{mL}$, $v = 200\,\text{m/s}$, $P_{max} = 1.2\,\text{kW}$ (b). The chosen configuration for further cogging force optimization is labeled with a red star in (a), and annotated in both graphs.

The global optimization for $V = 1\,\text{mL}$, $v = 200\,\text{m/s}$, $P_{max} = 1.2\,\text{kW}$ and stated constraints is an underhung motor with $N_C = 4$, $N_M = 9$, $L_k = 32\,\text{mm}$, $r_{mi} = 2\,\text{mm}$, $r_{mo} = 7.8\,\text{mm}$, $r_{ci} = 9.1\,\text{mm}$, $r_{co} = 13.1\,\text{mm}$, $r_{fi} = 13.2\,\text{mm}$, $r_{fo} = 13.93\,\text{mm}$, $\delta = 0.258$ and $M = 322\,\text{g}$. The plot in Fig. 4(b) illustrates that, at $N_C = 4$ at $N_M = 9$, the optimization algorithm found the most efficient motor configuration based on the input constraints. Furthermore, it appears to reach the optimization solution rather gradually and exhibit a noticeable degree of field convexity, which agrees with our assumption earlier.

Considering a motor with $L_s = 80\,\text{mm}$ acting upon a 1 mL ampoule with an orifice diameter of $200\,\mu\text{m}$ to generate jet velocity of $200\,\text{m/s}$, the motor is required to output 250 N at

(a) Cogging force optimization setup
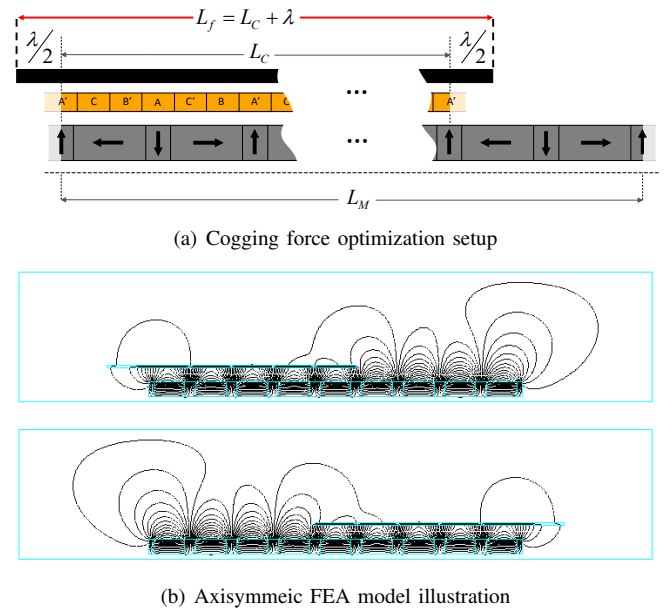

(b) Axisymmeic FEA model illustration

Fig. 5. Cogging force optimization with extended back-iron length $L_f = L_C + \lambda$, where λ is extra back-iron length, Δ is motor axial position in (a); and axisymmetric FEA model to work out cogging force for each L_f over the range of $\Delta = 0 \rightarrow L_s$ with no applied current in (b).

a stroke velocity of $0.5\,\text{m/s}$. The analytical model estimates the dimensionless motor constant $\hat{K}_m$ to be 0.1107, while the single coil pole/single magnet pole FEA model, similar to that in [10], is in strong agreement with the computed $\hat{K}_{m(FEA)}$ of 0.1149. Upon fulfilling all requirements and FEA validation, this motor configuration was chosen for further cogging force investigation before advancing to the final design.
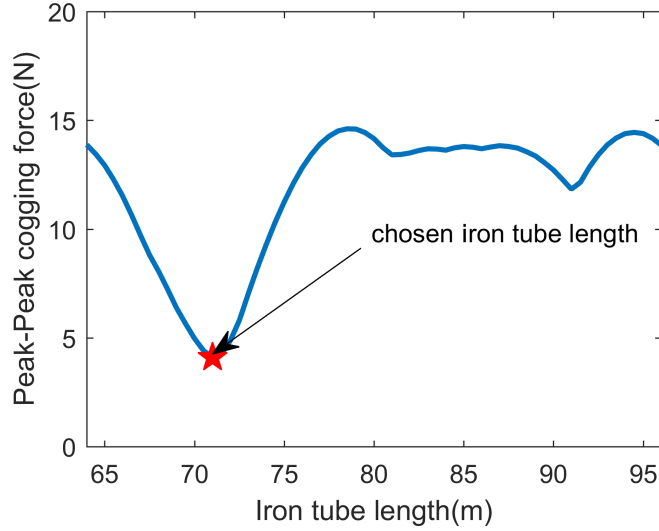
D. Cogging force optimization

By design intention, the back-iron tube does not cover the whole length of the Halbach magnet array. Thus, the motor is prone to problems related to end effect cogging force such as control instability. To reduce the magnitude of the cogging force, an FEA setup as illustrated in Fig. 5(b) was used to search for an alternative back-iron length that yields the least peak to peak cogging force.
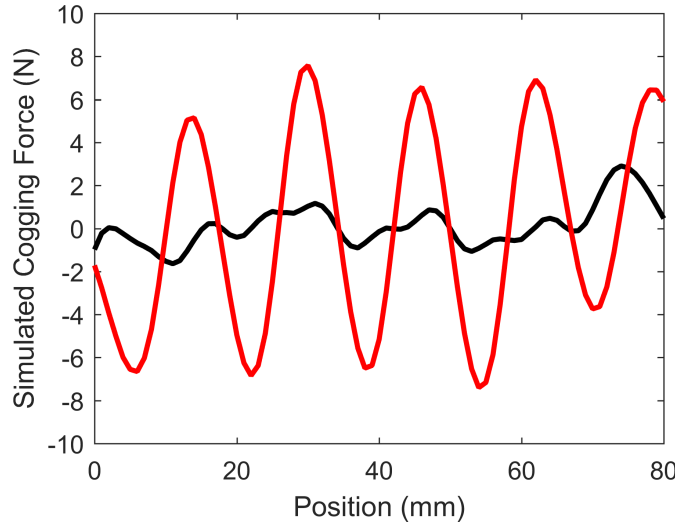
The cogging force optimization process was started by creating a base ANSYS Mechanical APDL script that describes the motor configuration obtained from the previous optimization. The model included additional parameterization of sleeve length λ and coil position Δ while excluding the conductor and input current conditions, as illustrated in Fig. 5(b). We created a Python automation script to collect axial forces acting on the back-iron F_c, then changed λ and Δ accordingly to repeatedly call the APDL batch process for the same base script. The automation script split the job into 5-6 concurrent threads which called independent APDL batch processes to fully exploit the available computing power.

The chosen motor configuration consists of four half-coil-poles with the minimum back-iron length $L_f = 64\,\text{mm}$. The automation script swept for extra back-iron lengths of

$\lambda = 0 \rightarrow 32\,\text{mm}$, with increment of $\text{d}\lambda = 0.5\,\text{mm}$, over the entire stroke length of $\Delta = 0 \rightarrow 80\,\text{mm}$, with increment of $\text{d}\Delta = 0.5\,\text{mm}$. We chose the back-iron tube length to be $L_f = 71\,\text{mm}$ for having the least peak to peak cogging force $\text{Max}(F_C) - \text{Min}(F_C) = 4.07\,\text{N}$. The chosen back-iron length of $L_f = 71\,\text{mm}$ reduces cogging force $71.5\,\%$ compared to the minimal choice of $L_f = L_C = 64\,\text{mm}$, as shown in Fig. 6(a). With a maximum FEA axisymmetric grid size of $0.5\,\text{mm}$, the whole process took 14 hours on an Intel i7 - 4970 CPU.

TABLE II
SUMMARY OF MOTOR DESIGN VALUES

Parameter	Description	Values
N_M	Number of half magnet-poles	9
N_C	Number of half coil-poles	4
r_{mi}	Magnet array inner radius	2 mm
r_{mo}	Magnet array outer radius	7.8 mm
r_{ci}	Coil array inner radius	9.1 mm
r_{co}	Coil array outer radius	13.1 mm
r_{fi}	Iron tube inner radius	13.2 mm
r_{fo}	Iron tube outer radius	13.93 mm
δ	Ratio of radial magnet vs. magnet pair	0.258
L_k	Repeat length	64 mm
L_M	Magnet array total length	144 mm
L_C	Coil array total length	64 mm
L_f	Iron tube length	71 mm
L_s	Stroke length	80 mm

IV. CONSTRUCTION & EXPERIMENTAL VALIDATION

A. Motor construction

Based upon the results of these optimizations obtained in Section III-C and summarized in Table II, we constructed a prototype motor and jet injector structure presented in [9] and

(a) Searching for L_f which yields the least cogging

(b) Predicted F_C at $L_f = 71\,\text{mm}$ (red) and $L_f = 79\,\text{mm}$ (black)

Fig. 6. Peak to peak cogging force $Max(F_C) - Min(F_C)$ against iron length $\lambda = 64 \rightarrow 96\,\text{mm}$, using the globally optimized motor configuration, with each point collected by moving back-iron over the entire stroke length L_s in (a); and comparison between the cogging force distributions of the worst-case iron length $L_f = 79\,\text{mm}$ (black) and the chosen $L_f = 71\,\text{mm}$ (red) in (b).
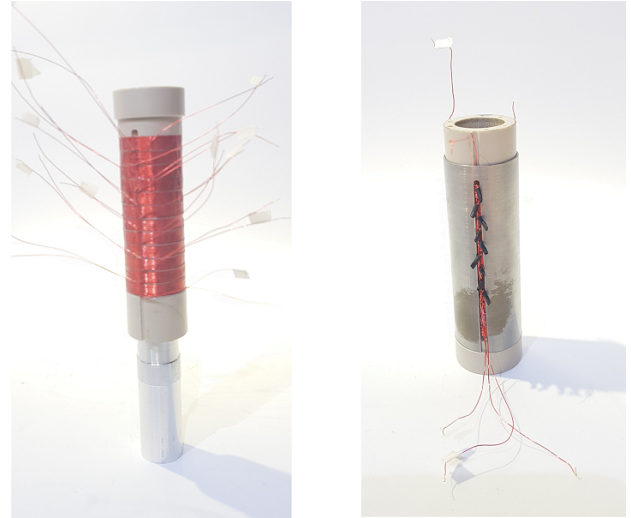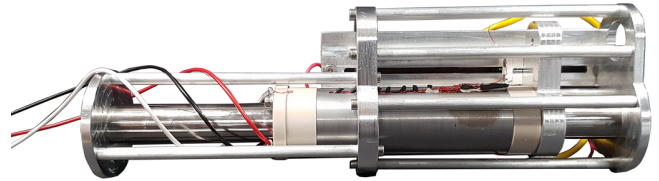

(a) The bobbin with fully wound coil (left) & iron tube assembly (right)

(b) Full motor assembly without the ampoule

Fig. 7. Pictures showing progress of the device construction: the bobbin with a fully wound coil, as well as the bobbin with coil and iron tube assembly (a); and the full motor assembly without the NFJI ampoule and casing (b).
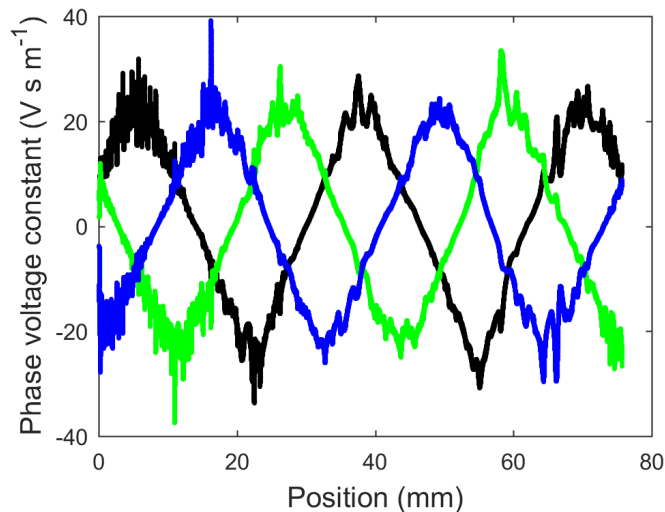
Fig. 8. Measured phase voltage constant K_e against motor position for each motor phase, determined over multiple passes at different velocities between $10\,\mathrm{mm/s}$ and $25\,\mathrm{mm/s}$. There is a range in velocity because the coil was moved by hand.
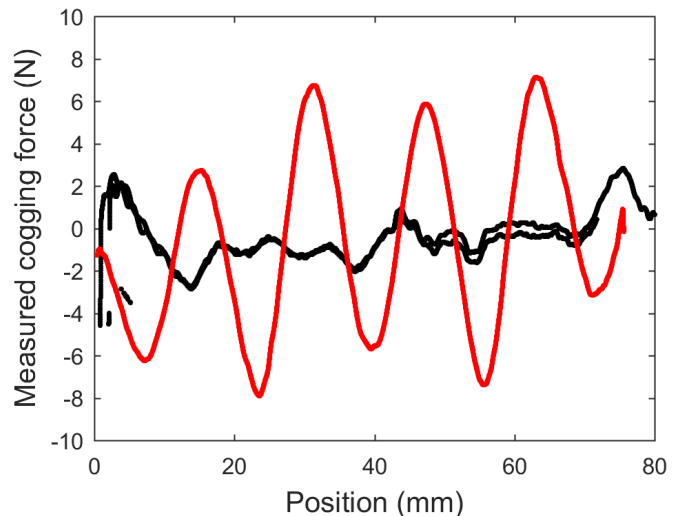
Fig. 9. Measured cogging force due to finite back-iron length, for a back-iron length of $79\,\mathrm{mm}$ (red) and a length of $71\,\mathrm{mm}$ (black). Position is measured relative to one end of the motor stroke.

shown in Fig. 7. In this prototype, each phase coil was wound using 180 turns of 28.5 AWG wire; four coils were joined in series to form each phase, with a phase resistance of $11.6\,\Omega$. The back-iron was provided with a $2\,\mathrm{mm}$ slit to facilitate electrical connection; narrow slits of this sort have been shown to have negligible effect on motor performance, and may have advantageous effects in reducing eddy currents [18]. In this initial prototype, a back-iron length of $79\,\mathrm{mm}$ was chosen, so as to explore the properties of a high-cogging-force regime, as well as the optimal length of $71\,\mathrm{mm}$.

The magnets (Grade N45SH, K&J Magnetics) were assembled inside a stainless steel tube ($16\,\mathrm{mm}$ outside diameter), with the radial magnets provided as four uniformly-magnetized segments. In addition to containing the repulsive forces acting upon the radial magnet segments, this tube also served as a bearing surface for polymer sleeve bearings integrated into the ends of the bobbin.

The motor was integrated into an injector structure parallel and adjacent to the drug ampoule, yielding a compact arrangement. This configuration requires the motor bearings and connecting structures to resist a moment, requiring the widely-spaced bearings and the use of a thick force-transmitting plate between the piston and the coil. A linear potentiometer (Bourns PTB) was used for absolute motor position measurement. As shown in Fig. 7(b), the motor and structure have a mass of $605\,\mathrm{g}$.

B. Motor constant measurement

The motor constant was evaluated by measurement of the phase back-EMF during externally-induced motion plotted on Fig. 8, with the phases connected in a wye topology. A load cell (Futek LCM300, $250\,\mathrm{lb}$. capacity) was used to simultaneously determine the cogging force exhibited by the prototype.

The measured voltage constants for the three phases are shown in Fig. 8. The relatively narrow radial magnets and close proximity of iron yield a triangular flux waveform, with minimal end effects; noise near the peaks is likely a result of the relatively slow movement velocity employed ($\sim 0.1\,\mathrm{m/s}$).

Based upon these voltage constants and the phase resistance, the motor constant is $6.6\,\mathrm{N}/\sqrt{\mathrm{W}}$, within $10\,\%$ of the design value of $7.2\,\mathrm{N}/\sqrt{\mathrm{W}}$. This would correspond to an operating power of $1.4\,\mathrm{kW}$, rather than the design point of $1.2\,\mathrm{kW}$. The reduced performance seen in the prototype appears to be due largely to a reduced winding fill factor from that which was expected, and may be improved by improved winding and interconnection technique.

C. Cogging force measurement

The measured cogging force is shown in Fig. 9, after correcting for bearing friction of $4.2\,\mathrm{N}$. The peak-to-peak amplitude for the $79\,\mathrm{mm}$ back-iron is approximately $14\,\mathrm{N}$, and for the $71\,\mathrm{mm}$ back-iron is $4\,\mathrm{N}$, in close agreement with the predictions shown in Fig. 6(b). There is also good agreement in the details of the cogging force waveform, with slight differences near one end of the stroke.

D. Needle-free Jet Injection

The other key component in a practical injection system is the power electronic drive, which needs to provide a burst of high power for a short time from a compact package. We have recently reported on such a system designed for a voice coil actuator [17]. The newest iteration of the device was built to be capable of three-phase drive to control the prototype motor for NFJI.

To validate the practical performance of the motor in performing needle-free jet injections, we inserted into it an ampoule and orifice, and estimated the velocity of the jet produced by directing it against a piezoelectric force sensor
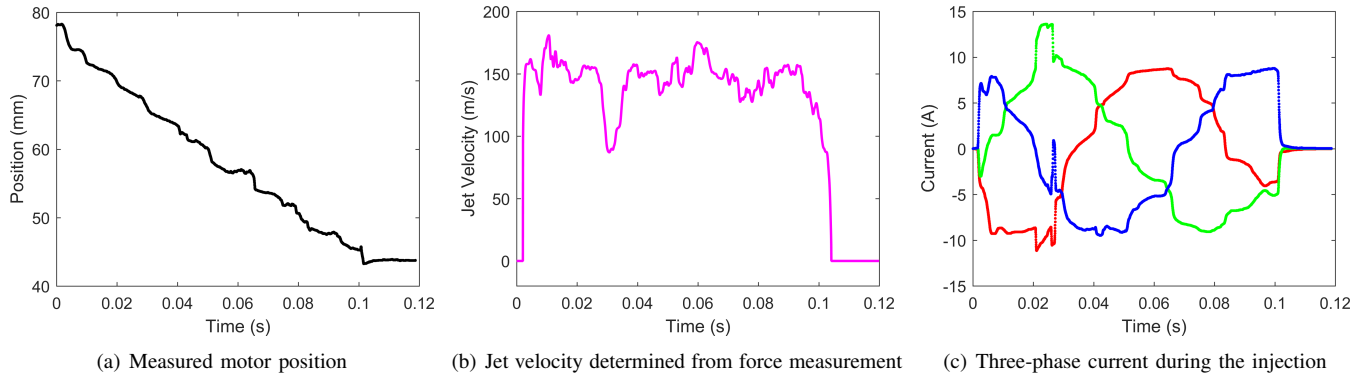
(a) Measured motor position   (b) Jet velocity determined from force measurement   (c) Three-phase current during the injection

Fig. 10. Measured piston position for a constant-voltage injection corresponding to a nominal power of 1.4 kW (a); the jet velocity determined from the force of the water jet acting upon the force sensor (b); and the current profile across the motor phases during the injection (c).
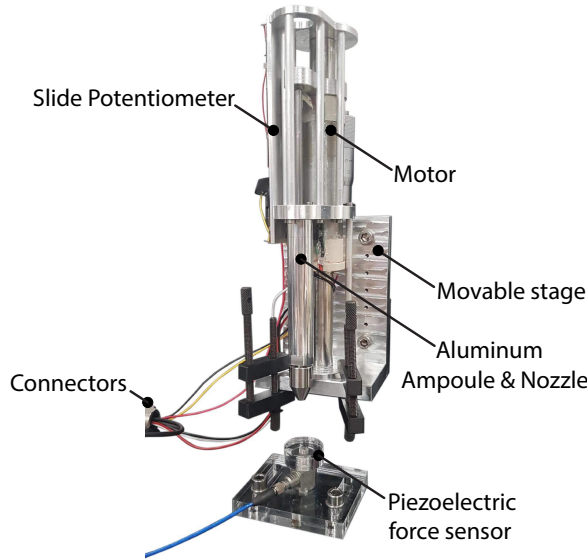

Fig. 11. Experimental setup in which the motor ejects water onto a piezoelectric force sensor, driven with constant motor input voltage

(model 208C01, PCB Piezotronics). By measuring the jet velocity in this way, we eliminate any potential effects from leakage or fluid compression. In Fig. 11, the experimental setup comprises the fully assembled motor mounted on a movable stage, with an aluminum ampoule filled with water pointing at the force sensor, and the power system to drive the motor (not shown here). Fig. 10 shows the results for a water jet ejection onto the force sensor placed $15\,\mathrm{mm}$ away from the tip of the nozzle. The controller applied a constant phase voltage amplitude of $110\,\mathrm{V_{rms}}$, corresponding to a nominal power of $1.4\,\mathrm{kW}$, for a period of $0.1\,\mathrm{s}$. Based on the measured travel distance of the motor piston, as shown in Fig. 10(a), the average jet speed achieved was $134\,\mathrm{m/s}$. This value is obtained from the relationship between the piston tip velocity v_{piston} and the water jet velocity v_{jet}, assuming an incompressible fluid and uniform plug flow:

$$v_{jet} = v_{piston} \frac{A_{piston}}{A_{jet}} \tag{22}$$

where A_{piston}, and A_{jet} are the cross sectional area of the piston, and jet nozzle, in the same order. Furthermore, the instantaneous force F_{ins} measured by the piezoelectic force sensor can be also translated to jet velocity v_{jet}, given A_{jet}, and known density of water ρ_{water}, assuming a uniform plug flow:

$$v_{jet} = \sqrt{\frac{F_{ins}}{\rho_{water} A_{jet}}} \tag{23}$$

The average jet speed calculated from the force measurement was slightly higher than the jet speed estimated by the position profile, at $144\,\mathrm{m/s}$. This is likely because the flow exiting the nozzle does not have a uniform velocity profile, which tends to increase the apparent jet speed obtained via force measurement. These jet speeds are well within the range of speeds useful in jet injection, and in line with other jet speeds obtained with this nominal pressure [19].

Despite the use of an open-loop, constant-voltage-amplitude control approach, the jet speed was relatively steady throughout the stroke, and most variations observed correspond to changes in the friction and cogging forces. The dip in velocity near the beginning of the injection may be due to the fact that during the loading process, an air bubble made its way into the ampoule. When the bubble approaches the output nozzle, the lack of fluid can cause sudden changes in velocity. Air bubbles can only be avoided through careful filling procedures.

These results validate that the prototype motor is capable delivering large volume needle free jet injection (up to $1\,\mathrm{mL}$) when given $1.4\,\mathrm{kW}$ of electrical power, close to the theoretical design value of $1.2\,\mathrm{kW}$. Improvements to the motor control strategy will allow for further enhancements to injection consistency and repeatability.

V. CONCLUSION

To summarize, we presented a semi-analytical solution for the electromagnetic model of slotless tubular LPMSMs, an efficient optimization scheme for the motor mass at a given

power dissipation, as well as an automated routine for estimating cogging force using FEA. Utilizing these modeling and optimization methodologies, we found a globally optimized motor configuration for NFJI that is complemented by an iron length that produces the minimal amount of cogging. The motor was designed to deliver $1\,\mathrm{mL}$ NFJIs, at rated motor speed of $0.5\,\mathrm{m/s}$, rated force of $250\,\mathrm{N}$, and rated electrical power requirement of $1.2\,\mathrm{kW}$. The optimized motor configuration for these requirements is summarized in Table II.

The measured motor constant, peak-to-peak cogging force, and bearing friction of the prototype motor constructed corresponding to the optimized design were $6.6\,\mathrm{N}/\sqrt{\mathrm{W}}$, $4\,\mathrm{N}$ and $4.2\,\mathrm{N}$, respectively. In a test injection provided with $1.4\,\mathrm{kW}$ of electrical power, the prototype motor produced a $200\,\mu\mathrm{m}$ thin jet of water into a force sensor with an average jet velocity of $134\,\mathrm{m/s}$, well within the practical jet injection velocity range [1]. Thereby, this prototype successfully demonstrated the capability for large volume needle-free jet injection. Future efforts will be aimed at improving the usability of the motor hand piece by creating a complimentary power device that is portable, and capable of powering multiple injections per recharge. Alternative control algorithms can be explored to improve the motor control performance. It is also worth mentioning that it is possible for the prototype motor to employ a compound ampoule similar to that reported in [7], [20], making the device capable of delivering close to $4\,\mathrm{mL}$ of liquid drug, and thus surpassing the volume needed for most protein based formulations [4].

In conclusion, the design methodology described in this work illustrates the benefits from considering the design of the actuator and its load simultaneously; a motor designed to fit an existing drug ampoule would exhibit significantly worse performance. Any piston pressurizing a fluid and powered by a LPMSM benefits from a reduction in diameter and increase in stroke length for a constant swept volume, which may prove useful in general fluid-handling, hydraulic, and pneumatic systems. Similar benefits may be possible in the design of actuated linkages, such as robot arms and powered exoskeletons.

ACKNOWLEDGMENT

REFERENCES

[1] S. Mitragotri, "Current status and future prospects of needle-free liquid jet injectors," *Nature Reviews Drug Discovery*, vol. 5, pp. 543–548, 2006.

[2] A. Taberner, N. C. Hogan, and I. W. Hunter, "Needle-free jet injection using real-time controlled linear Lorentz-force actuators," *Medical Engineering & Physics*, vol. 34, no. 9, pp. 1228–1235, 11 2012.

[3] B. D. Hemond, A. Taberner, C. Hogan, B. Crane, I. W. Hunter, and H. I. W., "Development and Performance of a Controllable Autoloading Needle-Free Jet Injector," *Journal of Medical Devices*, vol. 5, no. 1, p. 015001, 2013.

[4] N. C. Hogan, A. J. Taberner, L. A. Jones, and I. W. Hunter, "Needle-free delivery of macromolecules through the skin using controllable jet injectors," *Expert Opinion on Drug Delivery*, vol. 12, no. 10, pp. 1637–1648, 10 2015.

[5] B. P. Ruddy, I. W. Hunter, and A. J. Taberner, "Optimal voice coil actuators for needle-free jet injection," in *2014 36th Annual International Conference of the IEEE Engineering in Medicine and Biology Society*. IEEE, 8 2014, pp. 2144–2148.

[6] B. P. Ruddy, A. J. Taberner, and J. Boyce-Bacon, "Optimization of linear permanent magnet synchronous motors for needle-free jet injection," in *2015 Intl Aegean Conference on Electrical Machines & Power Electronics (ACEMP), 2015 Intl Conference on Optimization of Electrical & Electronic Equipment (OPTIM) & 2015 Intl Symposium on Advanced Electromechanical Motion Systems (ELECTROMOTION)*. IEEE, 9 2015, pp. 375–381.

[7] B. P. Ruddy, J. W. Mckeage, R. M. J. Williams, P. M. F. Nielsen, and A. J. Taberner, "A compound ampoule for large-volume controllable jet injection," in *2015 37th Annual International Conference of the IEEE Engineering in Medicine and Biology Society (EMBC)*, vol. 2015. IEEE, 8 2015, pp. 7341–7344.

[8] J. Schramm-Baxter and S. Mitragotri, "Needle-free jet injections: Dependence of jet penetration and dispersion in the skin on jet power," *Journal of Controlled Release*, vol. 97, no. 3, pp. 527–535, 2004.

[9] N. N. L. Do, A. J. Taberner, and B. P. Ruddy, "Design of a linear permanent magnet synchronous motor for needle-free jet injection," in *2017 IEEE Energy Conversion Congress and Exposition (ECCE)*. IEEE, 10 2017, pp. 4734–4740.

[10] B. P. Ruddy and I. W. Hunter, "Design and optimization strategies for muscle-like direct-drive linear permanent-magnet motors," *The International Journal of Robotics Research*, vol. 30, no. 7, pp. 834–845, 6 2011.

[11] J.-M. Jin, *The Finite Element Method in Electromagnetics*, 3rd ed. Wiley-IEEE Press, 2014.

[12] J. Wang, G. W. Jewell, and D. Howe, "A General Framework for the Analysis and Design of Tubular Linear Permanent Magnet Machines," *IEEE Transactions on Magnetics*, vol. 35, no. 3, pp. 1986–2000, 1999.

[13] N. Bianchi, "Analytical field computation of a tubular permanent-magnet linear motor," *IEEE Transactions on Magnetics*, vol. 36, no. 5 II, pp. 3798–3801, 2000.

[14] Wijono, H. Arof, and H. Ping, "Analysis of magnetic field distribution of a cylindrical discrete Halbach permanent magnet linear generator," *IET Electric Power Applications*, vol. 4, no. 8, p. 629, 2010.

[15] L. Yan, L. Zhang, T. Wang, Z. Jiao, C.-Y. Chen, and I.-M. Chen, "Magnetic Field of Tubular Linear Machines with Dual Halbach Array," *Progress In Electromagnetics Research*, vol. 136, no. November 2012, pp. 283–299, 2013.

[16] K. J. Meessen, J. J. H. Paulides, and E. A. Lomonova, "Analysis of 3-D Effects in Segmented Cylindrical Quasi-Halbach Magnet Arrays," *IEEE Transactions on Magnetics*, vol. 47, no. 4, pp. 727–733, 4 2011.

[17] B. Ruddy, A. Dixon, R. Williams, and A. Taberner, "Optimization of portable electronically-controlled needle-free jet injection systems," *IEEE/ASME Transactions on Mechatronics*, vol. 4435, no. c, 2017.

[18] K. J. Meessen, J. J. Paulides, and E. A. Lomonova, "Analysis and design of a slotless tubular permanent magnet actuator for high acceleration applications," *Journal of Applied Physics*, vol. 105, no. 7, pp. 1–4, 2009.

[19] R. M. J. Williams, B. P. Ruddy, N. C. Hogan, I. W. Hunter, P. M. F. Nielsen, and A. J. Taberner, "Analysis of Moving-Coil Actuator Jet Injectors for Viscous Fluids," *IEEE Transactions on Biomedical Engineering*, vol. 63, no. 6, pp. 1099–1106, 6 2016.

[20] J. W. McKeage, B. P. Ruddy, P. M. Nielsen, and A. J. Taberner, "Power-efficient controlled jet injection using a compound ampoule," *Journal of Controlled Release*, 2018.